

Research Article

Optoelectronic Heating for Fabricating Microfluidic Circuitry

Gauvain Haulot and Chih-Ming Ho

Mechanical and Aerospace Engineering Department, University of California, Los Angeles, Los Angeles, CA 90095, USA

Correspondence should be addressed to Chih-Ming Ho, chihming@seas.ucla.edu

Received 7 June 2011; Accepted 1 August 2011

Academic Editor: Eric Pei Yu Chiou

Copyright © 2011 G. Haulot and C.-M. Ho. This is an open access article distributed under the Creative Commons Attribution License, which permits unrestricted use, distribution, and reproduction in any medium, provided the original work is properly cited.

This work reports on optoelectronic-based heaters that can transduce low-power optical images into high-power heating to melt frozen liquids and form desired microfluidic circuitry. The mechanism of optoelectronic heating (OEH) was studied and characterized. OEH relies on photocurrent heating in the illuminated parts of actuating images. Resolution was affected by dark current heating. Photocurrents and dark currents were measured and related to the operating parameters. Successful melting of a frozen media within seconds with 2 mW light patterns and a 4 V operating voltage was demonstrated with feature sizes down to $200\ \mu\text{m} \times 200\ \mu\text{m}$. Strategies to increase resolution were addressed. It was shown that the size and location of heating areas can be reliably and rapidly reconfigured by changing the actuating image.

1. Introduction

Microelectromechanical system (MEMS) techniques have enabled thermal control at the microscale and thereby opened up the way to new applications. Microheating has been applied to various chemical and biological processes [1, 2], where accurate control of temperature is often essential, with a particular focus on polymerase chain reaction [3]. It has also been popular for microfluidic flow control; thermal pumps [4] and valves [5] offer elegant solutions for device integration. They are based on thermal expansion or phase transition of specific materials. Other thermal phenomena include the control of viscosity for droplet generation [6], temperature gradient focusing of particles [7], and thermocapillary pumping [8]. Local microheating is usually achieved with thin-film resistive heaters that are deposited and patterned using MEMS fabrication techniques. Optical heating is a convenient alternative.

Existing optical heating often requires a high-power light source and has been successfully demonstrated in chemical and biological applications [9, 10]. Optothermal valves and pumps have also been implemented in microfluidic platforms [11, 12]. They are typically based on thermal expansion of bubbles or nanocomposite materials in prefabricated areas. Biocompatible thermoreversible gelation polymers

offer more flexibility [13]. Those polymers solidify when heated and are biocompatible. They can be mixed with biochemical samples and be used as ubiquitous valves activated upon irradiation [14]. Nonetheless, all those devices are reliant on the optical absorption of liquids, which varies with chemical composition. Photoabsorbing substrates are a convenient alternative. They have been applied to optothermal valves [15] and droplet manipulation based on thermocapillary effects [16].

Optical actuation with low-power light patterns has been recently developed for microfluidics. It offers significant advantages for device integration and parallel manipulation. It is based on optoelectronic amplification of optical signals. So far, it has mainly relied on dielectrophoresis, with the optoelectronic tweezers (OETs) [17], and on optoelectrowetting [18].

In this work, optical actuation with low-power light is extended to microheating. Optoelectronic heating (OEH) constitutes a new technique for thermal control at the microscale. OEH provides high flexibility in thermal operations and is of particular interest for microfluidic applications, especially in the area of phase-transition-based flow control [19]. This paper reports on the fabrication and characterization of newly developed optoelectronic heaters (OEH devices).

2. Device Physics and Structure

The device presented in this work enables local microheating controlled by low-power light images. Such process is illustrated in Figure 1. Images are generated by a DMD microdisplay (DMD Discovery 1100 by Texas Instruments) and are projected onto an OEH device. Based on an optoelectronic heating transduction process, OEH devices convert the lighted parts of an image into heating areas. OEH is based on a photoconductive material sandwiched between two electrodes. The bottom electrode is made of transparent indium tin oxide (ITO). The top electrode is highly reflective and contains silver. A voltage bias is imposed between the electrodes, which induces a vertical electric field across the photoconductor. The lighted areas of displayed images create charge carriers in the photoconductive layer that are accelerated by the electric field; they produce heat by the Joule effect. Thus, only low optical power is needed.

The photoconductive layer must absorb light efficiently and thus necessitates a minimum thickness. Meanwhile, lateral heat transfers must be minimized for high resolution; this is why a thin film with low thermal conductivity is required. Hydrogenated amorphous silicon (a-Si:H) meets both those requirements. One-micrometer films can absorb light efficiently (absorption is 10^{-4} cm^{-1} at 630 nm), and its thermal conductivity is low, reportedly between 0.1 W/m/K [20] and 2.6 W/m/K [21] (this last value was measured in pure amorphous silicon films). In comparison, crystalline silicon (cSi) layers must be $30 \mu\text{m}$ thick to absorb light efficiently, and the material's thermal conductivity is approximately 140 W/m/K, leading to poor resolution.

The system's temperature is controlled by a cooler. The cooler is placed underneath the optoelectronic chip to keep the top surface clear for observation and to facilitate access to the OEH device for eventual applications. Since observation requires illumination that would interfere with the actuating light patterns, the patterns are projected from underneath the chip; the cooler thus needs to be transparent.

In the OEH device, heat is generated by the Joule effect. The heating power is defined as

$$P_{\text{heat}} = I \cdot V, \quad (1)$$

where I is electrical current and V is the voltage bias. Therefore, the device's performance is monitored with I - V curves. A typical I - V characteristic measured on an OEH device is plotted in Figure 2.

The total current is sum of the dark current and the photocurrent: $I = I_D + I_p$. Photocurrents are activated by the lighted parts of displayed images. Dark currents emerge from intrinsic properties of the photoconductor, from the dark parts of displayed images, and from light used for observation. A key feature of OEH is resolution, which stems from the difference between heat generated in the lighted areas of a displayed image and heat generated in the dark areas of the image. Therefore the effective heating power depends on the photocurrent, and heating resolution will be improved by reducing dark currents.

The device displays a rectifying behavior (Figure 2). It comes from the metal-semiconductor contact, or the

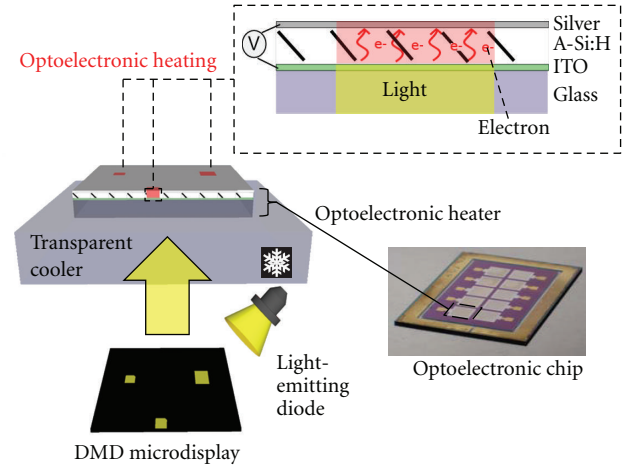


FIGURE 1: Structure and physics of the OEH platform.

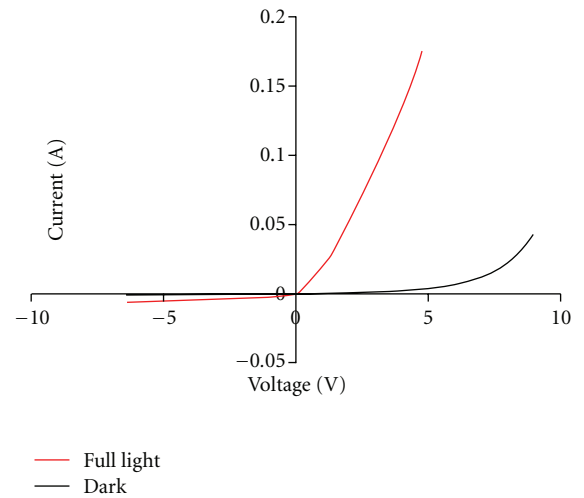


FIGURE 2: Typical I - V characteristic measured on an OEH device. “Full light” means that the device is lighted throughout its entire surface, and “dark” means that a black image is displayed. Forward/reverse bias (positive/negative voltage) corresponds to a negative/positive potential applied to the bottom ITO electrode.

Schottky contact, at the interface between a-Si:H and the silver electrode. Such contacts have been reported for a-Si:H and used for solar cell applications [22]. The a-Si:H layer is n-doped in the vicinity of its interface with ITO to ensure ohmic contact. Because forward bias (negative potential applied to the bottom electrode) by far gives the highest power output, OEH is performed under such a bias.

Dark currents are expected to be greatly influenced by the Schottky barrier, and photocurrents to a lesser extent. In spite of the fact that the Schottky barriers in a-Si:H have been extensively studied, they are usually investigated under reverse bias and low forward bias. Indeed, high forward bias tends to reduce such barriers: as the forward bias increases, the depletion region decreases. The barrier therefore eventually becomes negligible. Moreover, the series resistance of intrinsic hydrogenated amorphous silicon is high (mobilities are low). At higher voltage, currents become series-resistance

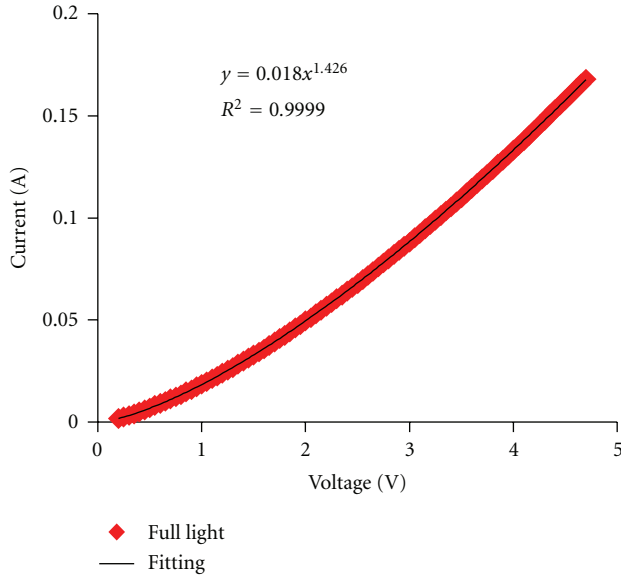


FIGURE 3: Photocurrent under forward bias for a fully lighted image (the entire surface of the OEH device is illuminated).

limited [23, 24], which precludes experimental studies of the barrier. It also entails high heat losses in the device, which is generally a drawback; in this work, it is the effect sought after.

3. Materials and Methods

OEH devices were fabricated from hydrogenated amorphous silicon chips purchased from Silicon Digital (Korea). Such chips consisted of a glass substrate, a 200 nm thick indium tin oxide (ITO) electrode, a 50 nm n-doped a-Si:H layer, and a 1 μm -thick intrinsic a-Si:H layer; they were 3 cm wide and 5 cm long. An array of 10 OEH devices was made out of one of those chips. 500 nm of silicon dioxide was deposited by plasma-enhanced chemical vapor deposition (PECVD) and subsequently patterned by wet-etching using buffer oxide etch (BOE, 6 : 1). SiO_2 filled possible pinholes in the a-Si:H film to prevent shunt currents. SiO_2 was etched in the future locations of the OEH devices and in the periphery. Amorphous silicon was then etched by RIE in the periphery in order to reveal the underlying ITO. Contact pads for the OEH devices' top electrode and for ITO were subsequently deposited by evaporation and patterned by liftoff. This layer was made of titanium and gold (10 nm and 100 nm). Finally, the OEH devices' top electrodes were deposited and patterned through the same process. They were made of titanium for adhesion (10 nm), platinum as an atomic diffusion shield that protected the semiconductor from silver (50 nm), and silver for high reflection (100 nm). A picture of the final chip is shown in Figure 1.

The chip was then placed on a cooler. The cooler was made of an aluminum plate with a built-in transparent sapphire window. Sapphire has a high thermal conductivity, which is essential to cooling efficiency. To limit light absorption while cooling homogeneously, the cooler's thickness was minimized based on simulations using the COMSOL

Multiphysics software. Temperature was controlled by thermoelectric coolers (PT8-25-40*80 by Melcor, Trenton, NJ, USA) attached to the aluminum plate.

A DMD microdisplay generated images that were focused on the photoconductive layer using lenses and a mirror (Thorlabs, Inc.). The DMD was integrated with a light source consisting of a red diode emitting at 629 nm and with a projection lens (ViALUX GmbH, Germany). This wavelength provided optimum absorption in the 1 μm thick a-Si:H layer. For most of the experiments, the chip was connected to an electrical setup controlled by LabView. I - V curves were plotted based on this setup. For melting experiments, however, a dc generator was directly connected to the chip. OEH devices were visualized through a microscope placed above the optoelectronic chip.

For the melting experiments, a layer of liquid hexadecane (ReagentPlus, 99%, Sigma-Aldrich) was placed on the optoelectronic chip at room temperature. The layer was confined using spacers and a glass cover slip. The cooler's temperature was then set to 288 K to freeze hexadecane. Using a 4 V operating voltage and images of square patterns, melting of square-shaped areas was achieved.

4. Experimental Section: Characterization of OEH

For high power and high resolution, heating must be maximized in lighted regions and minimized in dark regions. Photocurrents and dark currents are studied by using fully lighted images (the entire surface of the OEH device is illuminated) and black images, respectively. Furthermore, optical control of OEH is investigated using more complex light patterns.

4.1. Heating Power: Study of Photocurrents. In this section, photocurrents and their dependence on voltage and on the optical power input are investigated. Dark currents can be subtracted from the current measured under full illumination to study the photocurrents (see Figure 2). The resulting curve is plotted in Figure 3.

Theoretically, in a photoconductor, photocurrents are linearly correlated to voltage [25]. They follow the following equation:

$$I_P = (\mu_n + \mu_p) G_e \tau q \frac{A}{l} V, \quad (2)$$

where μ_n and μ_p are, respectively, the electron and hole mobilities, G_e is the carrier generation rate, τ is the carrier life time, q is the elementary charge, A is the illuminated photoconductor area, l is the semiconductor thickness, and V is the voltage bias. A slight nonlinear trend is observed in Figure 3 however. The plot is fitted for voltages greater than 0.3 V, since measurements at very low voltages are noisy. With excellent correlation of $R^2 = 0.9999$, the photocurrent follows the following equation:

$$I_P = I_{0P} V^\varphi \quad (3)$$

with $\varphi = 1.43$ and $I_{0P} = 1.85 \cdot 10^{-2} \text{A}$.

The exponent φ is greater than its theoretical value of 1 (see (2)). Such a superohmic photoconductivity has been reported in a-Si:H under high electric fields, typically above 10 kV/cm [26, 27], which is comparable to the ones used in the present study. This behavior, however, decreases with temperature, and those experiments were performed at 100 K and below. The Schottky contact is a more likely cause of superohmic photoconductivity in the present study. Since the depletion region at the corresponding metal-semiconductor interface decreases when forward bias increases, the series resistance is also reduced and thereby causes the observed superohmic trend.

A key aspect of OEH is its low-power light source. This feature is studied by measuring the power output under different optical power inputs. The results are represented in Figure 4(a).

Fully lighted images are displayed at different optical powers. In Figure 4(a), 100% corresponds to the maximum power output of the display system, 2 mW. Percentages of the maximum power are achieved by homogeneously turning off pixels in the projected image. Each millisecond, a new image with newly turned-on and turned-off pixels is displayed to ensure homogeneity. For that purpose, the DMD display is controlled by a Matlab program. I - V curves are plotted under optical powers varying from 10% to 100%, with 10% increments. A clear saturation trend is observed. It shows that increasing the optical power input above 1 mW (corresponding to 50%) has a limited impact on heat generation.

Those results can be analyzed using the equation found for photocurrents, (3). After subtracting the dark currents, which correspond to the 0% curve in Figure 4(a), excellent fitting is achieved, with R^2 values ranging from 1 to 0.9995 for light intensities above 20%. 10% light intensity gives $R^2 = 0.9988$. The corresponding values for I_{0P} and φ are plotted in Figures 4(b) and 4(c).

I_{0P} increases with the optical power input as illustrated in Figure 4(b), but a slight saturation tendency is observed. Figure 4(c) shows that increasing light intensity decreases φ , leading to a lower response to voltage. Figures 4(b) and 4(c) clearly indicate that photocurrents tend to saturate when the optical power increases.

Furthermore, theoretically I_{0P} is proportional to the carrier generation rate, which itself is proportional to light intensity. It comes from (2) and from the following equation for the generation rate [25]:

$$G_e = \frac{1}{Al} \eta \frac{P_{\text{opt}}}{h\nu}, \quad (4)$$

where η is the quantum efficiency, P_{opt} is the light intensity or incident optical power, and $h\nu$ is the photon energy. From the data displayed in Figure 4(a), photocurrents are plotted against light intensity for various values of the bias voltage (Figure 4(d)). According to Figure 4(d), photocurrents approximately scale with light intensity following a power law with exponent smaller than one:

$$I_P \propto P_{\text{opt}}^\gamma, \quad \text{with } \gamma < 1. \quad (5)$$

This behavior has been reported previously [28, 29]. The exponent γ is plotted in Figure 4(e). Interestingly, γ decreases with voltage. It shows that the dependence of photocurrents on voltage and their dependence on light intensity are correlated. The literature reports values of γ spanning from 0.5 to 1 [28, 29] depending on the recombination process. If recombination is purely bimolecular (involving an electron and a hole), $\gamma = 1/2$; if recombination is purely monomolecular (involving a single charge carrier at a time), $\gamma = 1$ [28].

These results show that photocurrents are related to voltage and light intensity through a power law, with a scaling exponent greater than one for voltage and smaller than one for light intensity. These relations are correlated, since the exponent of the power law for voltage (φ) depends on light intensity and the exponent of the power law for light intensity (γ) depends on voltage. Increasing voltage is an efficient way to achieve high-power OEH with low-power light. On the contrary, increasing the optical power input above the level currently available on the OEH platform will have little effect.

4.2. Resolution: Study of Dark Currents. Resolution is affected by heat generation in the dark areas of the displayed patterns. It stems from two sources: dark currents and background currents. Dark currents are generated by the voltage bias. They can result from thermal excitation of carriers or background doping in a-Si:H. Background currents are excited by background illumination, which comes from the light used for observation and from the dark parts of images. Black images indeed generate a $3 \mu\text{W}$ optical power. In this work, dark currents and background currents are grouped together and simply designated as dark currents to indicate that they occur in dark regions.

The forward characteristics of an OEH device are measured under complete dark at 22°C . To assess the influence of background currents, the characteristics are also measured when a black image is displayed and when the device is illuminated for microscope observation. The characteristics are fitted with the diode equation:

$$I_D = I_{0D} \left(\exp\left(\frac{qV}{nk_B T}\right) - 1 \right), \quad (6)$$

where V is the bias voltage, k_B is the Boltzmann constant, T is the temperature, and n is the ideality factor. The results are plotted in Figure 5. For complete dark, dark with DMD background light, and dark with background light and observation light, values for I_{0D} are, respectively, 5×10^{-5} A, 3.3×10^{-4} A, and 1.17×10^{-3} A. The corresponding values for n are 56, 69, and 79, respectively. Background and observation lights expectedly increase both I_{0D} and n . The diode model matches the data well. At 4 V, carriers generated by background light approximately result in a three-fold increase of current; adding microscope illumination causes another twofold.

The ideality factors are high compared to reported values. They are usually close to unity, although they can increase up to values of 10 at lower temperature [22, 30]. Nevertheless, values reported in previous works were measured at low

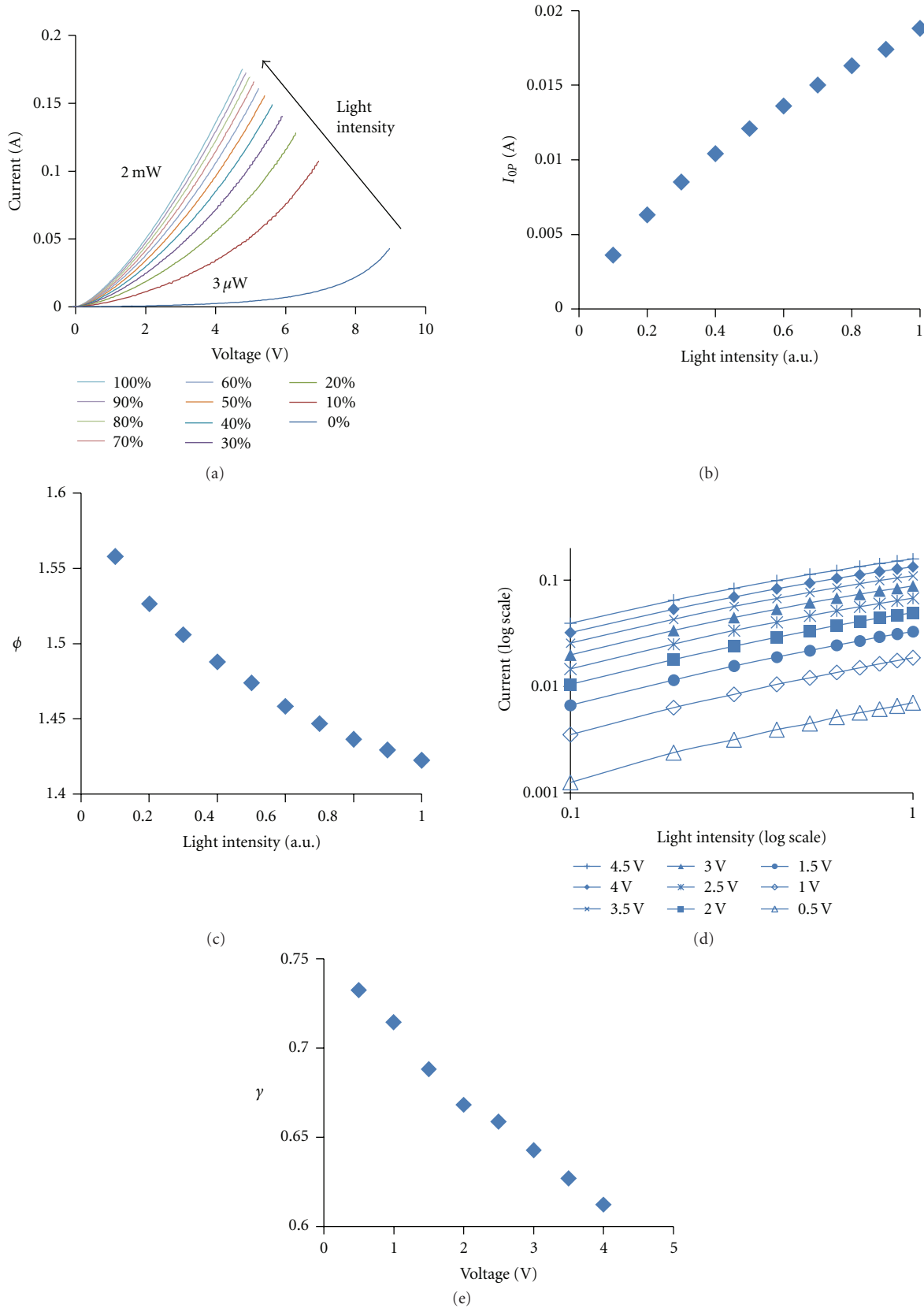


FIGURE 4: Influence of the optical power input on OEH. (a) $I-V$ curves showing the functional dependence of currents on light intensity under fully lighted images (the entire OEH device's surface is illuminated). Light intensities are indicated as percentages of the maximum light intensity (2 mW), with 10% increment. 0% ($3 \mu\text{W}$) corresponds to a black image. (b) and (c) Influence of light intensity on I_{0P} and ϕ defined in the photocurrent equation as $I_P = I_{0P}V^\phi$. (d) Current against light intensity for various values of the bias voltage (log-log scale). (e) Functional dependence of γ on voltage, where γ relates photocurrents to light intensity through the power law $I_P \propto P_{\text{opt}}^\gamma$.

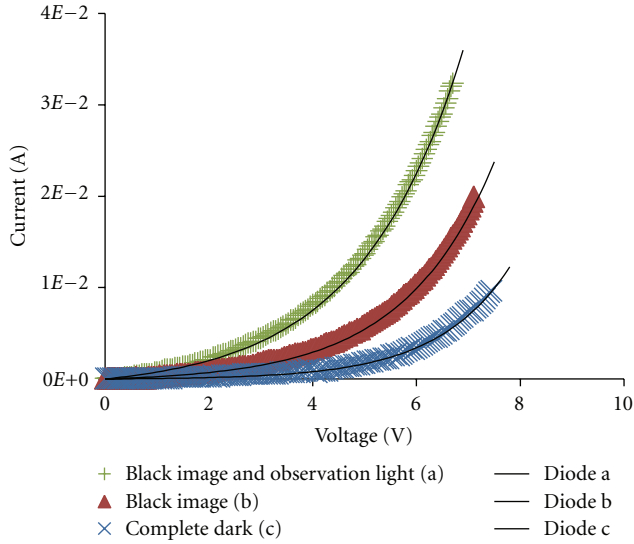


FIGURE 5: I - V curves for an OEH device under various “dark” conditions and their respective fittings. Fittings are based on the diode equation (6). Measurements are performed in complete dark (a), when a black image is projected onto the OEH device (b), and when a black image is displayed and the top electrode is illuminated for microscope observation (c).

voltages, typically between 0.2 V and 0.6 V (ideality factors close to unity cause the current to reach very high values around 1 V). On the contrary, the study herein investigates a voltage range between 0 V and 8 V. At such far forward bias, series resistance and, at higher voltages, eventual space-charge-limited currents have to be accounted for [23]. Those phenomena limit currents and explain high ideality factors. Furthermore, the prefactor I_{0D} is higher compared to reported values. It stems from high forward bias and shunt currents. Shunt currents are caused by pinholes in the photoconductive layer and have been reported in a-Si:H films [23].

Resolution can be increased by mitigating dark current heating. It can be done by reducing currents induced by microscope illumination. The related optical power can be reduced to a minimum value, or other visualization strategies can be adopted. Furthermore, observation light is partly reflected by the silver electrode, since the reflectance of silver is between 90% and 95% for most of the visual range of the light spectrum. Some of it is absorbed, however, which causes currents. Improving reflection of the OEH device’s top electrode, for instance, using antireflective coating, should therefore reduce dark heating. Filtering light to a particular range of wavelengths could also optimize reflection. On the contrary, not much can be done to curb background currents originating from the dark parts of displayed patterns. The only option is to use a display device with a higher contrast. Finally, dark currents that do not emerge from background light can be reduced using higher-quality materials, with minimal shunts and background doping. It will increase the series resistance.

For a heater, the effect of temperature variation on device performance is important. The characteristics of dark currents under background and observation light as well as

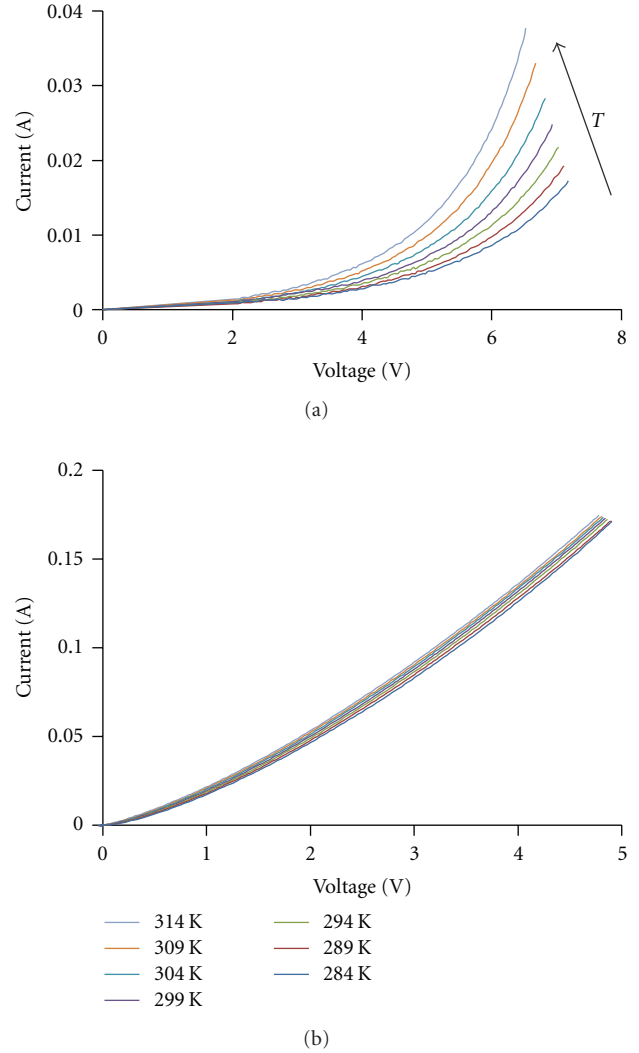


FIGURE 6: I - V curves showing the influence of temperature (T) on dark currents (a) and photocurrents (b). The increase of temperature is illustrated with an arrow.

the characteristics of photocurrents under full illumination are studied at different temperatures. The results are plotted in Figure 6. The temperature range studied spans from 284 K to 314 K. Temperature has a relatively stronger influence on dark currents than on photocurrents. It entails that, when temperature increases, heating power will be maintained but resolution will be affected. This effect is stronger at higher voltages.

4.3. Optical Control of OEH. Up to this point, only fully lighted and black images have been used to study the OEH device. The goal for OEH is to offer optically controlled microheating with high flexibility in terms of size, location, and timing. In this section heating is thus studied with more complex images: square patterns of different sizes in a fixed location, square patterns of fixed size in different locations, and finally sequences of fully lighted and black images with varying frequencies to investigate the device’s time response.

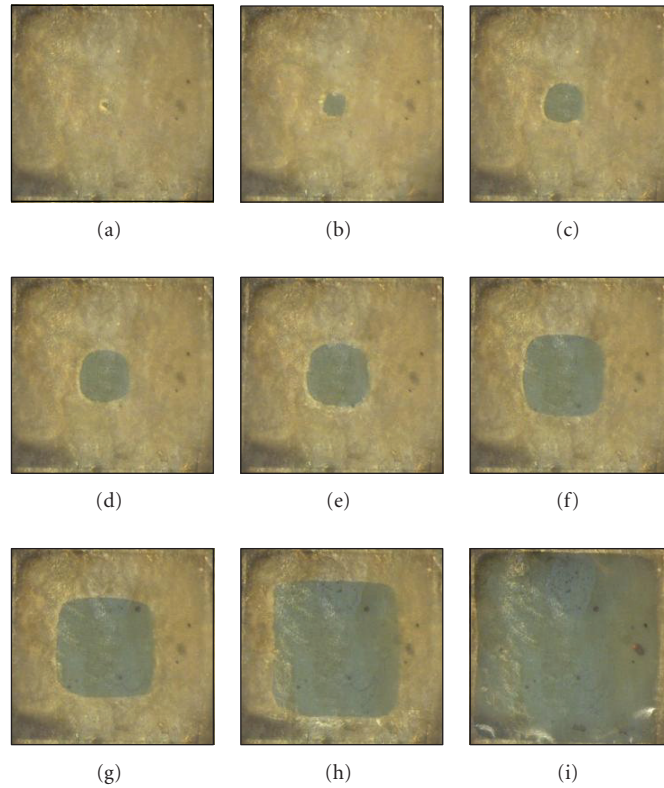


FIGURE 7: Melting of square-shaped areas localized at the OEH device’s center in hexadecane at 15°C. From (a) to (i) in percentage of chip area: 1%, 2.25%, 4%, 6.25%, 9%, 16%, 25%, 56.25%, and 100%. Each image represents a 5 mm × 5 mm area.

An interesting application of OEH is the rapid fabrication and reconfiguration of microfluidic structures by local thawing of a frozen media. Melting actuated by images is demonstrated herein. It is also a convenient way to visualize OEH. The melting material used is hexadecane. It melts at 18°C, and its latent heat is 184 kJ/L (as compared to 332 kJ/L for water). The system temperature is set at 15°C, and the operating voltage is 4 V. Square patterns of different sizes are displayed at the chip center. Figure 7 illustrates the experimental results.

Figure 7 shows square-shaped melted areas ranging from 500 μm × 500 μm to 5 mm × 5 mm. They were melted within seconds, thus proving OEH’s efficiency, and they remained stable thereafter. Steady state was achieved between 2 s and 10 s depending on the feature size—the transient time increased with size. For better visualization, a rather thick layer of hexadecane was used. The thickness was between 150 μm and 200 μm. Since melting was detected only when the layer was thawed throughout its whole thickness, smaller feature sizes were obtained with thinner films.

The melted areas display rounded corners. They are due to the isotropy of heat diffusion, as corroborated by three-dimensional simulations based on the COMSOL Multiphysics software. The simulations also show that temperature within the device does not vary more than a few degrees. Indeed, thermal insulation has not been optimized in this study. In particular, the high thermal conductivity of silver

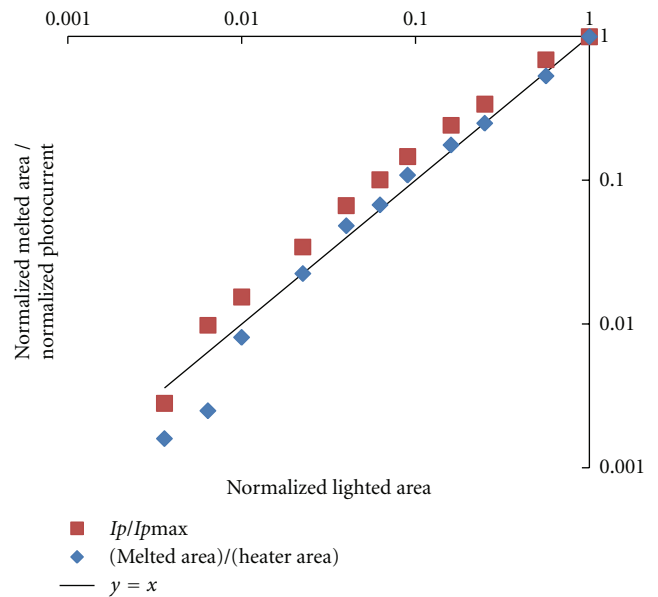


FIGURE 8: Functional dependence of normalized photocurrents and normalized melted areas on the corresponding normalized lighted areas. The expected linear trend is plotted for reference. Photocurrents are normalized to the photocurrent generated by a fully lighted image, where the entire OEH device area is lighted. Melted areas and lighted areas are normalized to the OEH device (heater) area.

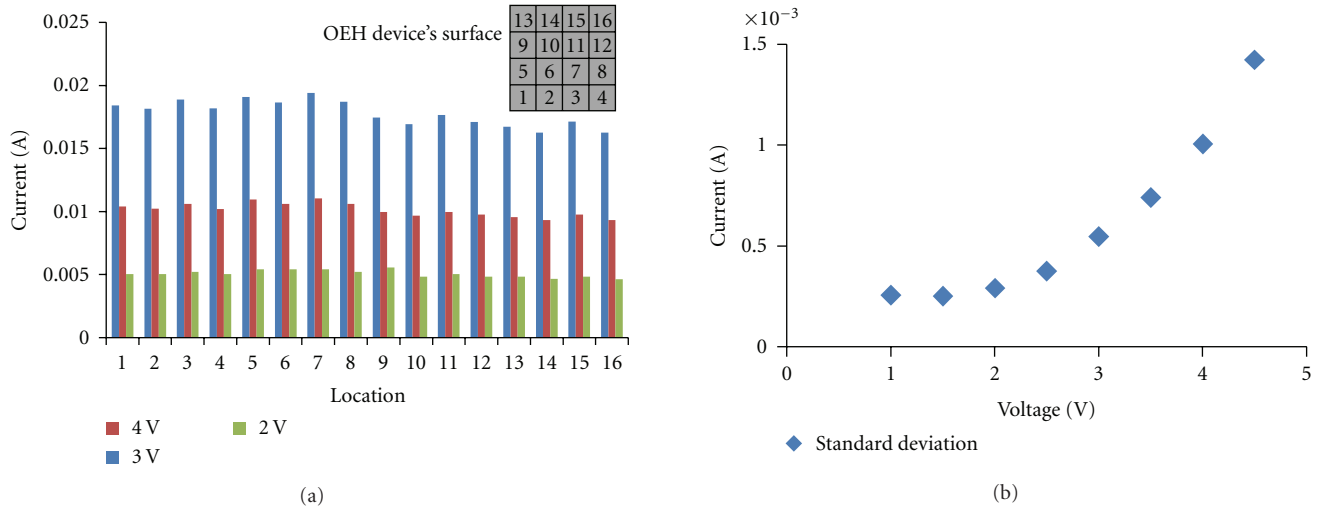


FIGURE 9: Homogeneity of photocurrent actuation throughout an OEH device's surface. (a) Current in 16 $1.25 \text{ mm} \times 1.25 \text{ mm}$ areas covering the entire surface of an OEH device at various voltages. The areas were lighted one at a time. (b) Standard deviation of current values throughout the 16 areas: functional dependence on voltage.

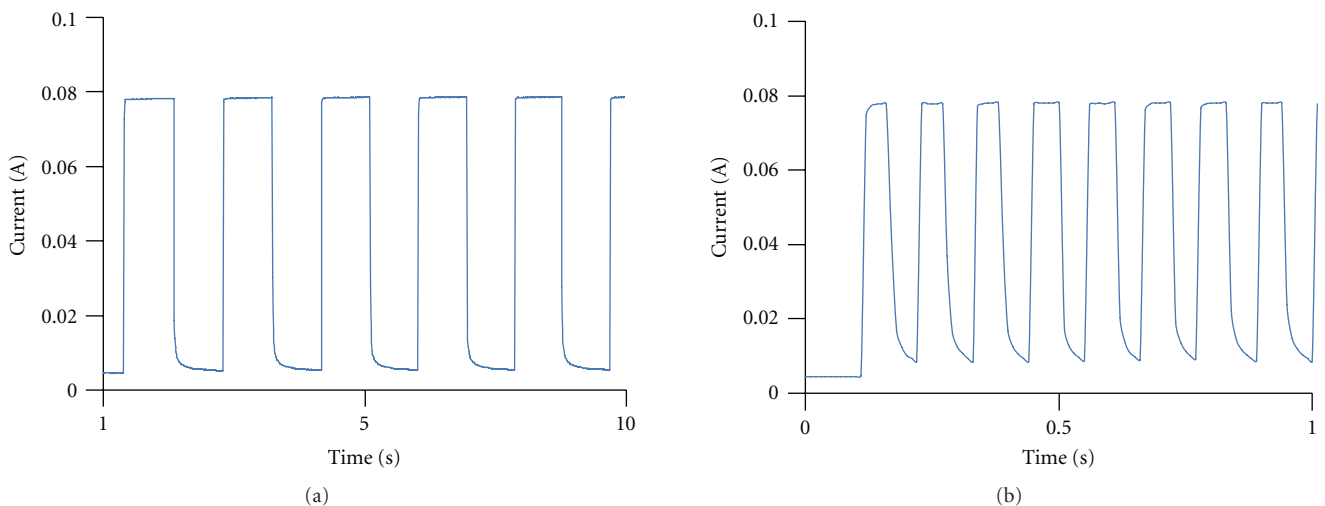


FIGURE 10: Current variation with time when a fully lighted image and a black image are sequentially displayed one after the other, each for 1 s (a) or for 0.05 s (b).

accounts for higher heat fluxes in the OEH device's top electrode.

More measurements were carried out with a $100 \mu\text{m}$ thick layer of hexadecane. Pictures of melted square patterns were taken and used to evaluate the corresponding areas. Normalized melted areas are plotted against the corresponding normalized lighted areas in Figure 8. Melted areas and lighted areas are normalized to the OEH device's surface area. Photocurrents were also measured. They are plotted against the corresponding normalized lighted areas in Figure 8. Photocurrents are normalized to the maximum photocurrent, which is activated by fully lighted images. Melted areas and photocurrents are accurately controlled by the light patterns down to $500 \mu\text{m} \times 500 \mu\text{m}$ features. The

preciseness and effectiveness of OEH are thereby demonstrated. Optical control becomes nonlinear below $500 \mu\text{m} \times 500 \mu\text{m}$ features. This phenomenon is observed on data points corresponding to melted areas of $200 \mu\text{m} \times 200 \mu\text{m}$ and $250 \mu\text{m} \times 250 \mu\text{m}$ that are actuated by square patterns of areas $300 \mu\text{m} \times 300 \mu\text{m}$ and $400 \mu\text{m} \times 400 \mu\text{m}$, respectively. As stated hereinbefore, the layer's thickness plays a role in this nonlinear behavior. Besides, dark currents become comparable to photocurrents at lower feature sizes. Thereby, the dark currents affect resolution and also account for this nonlinear response.

Figure 8 shows that for lighted areas larger than $500 \mu\text{m} \times 500 \mu\text{m}$ the photocurrent can be used as a proxy for OEH and for melting. It will be used in the following. Heating

homogeneity is important for the reliability of OEH devices. To test homogeneity, the OEH device's surface was divided into a four by four array of 16 $1.25\text{ mm} \times 1.25\text{ mm}$ areas. The areas were lighted one at a time, and the current was measured. The experiment was repeated at several voltages; the results for 2 V, 3 V and 4 V are plotted in Figure 9(a).

An OEH device is a square of area $5\text{ mm} \times 5\text{ mm}$ (cf. Figure 1). Figure 9(a) shows how heating varies throughout the OEH device's surface. Although the values are close to one another, differences appear. No obvious trend such as edge effects stands out however. The standard deviation for the current values throughout the 16 unit areas is plotted against voltage in Figure 9(b). Homogeneity in the areas' response to optical actuation is fairly good throughout the OEH device's surface: the standard deviation stays below 5% of the average value. The highest difference between current values, however, reaches 15%. The reason for this slight heterogeneity is not straightforward. A likely cause is the quality of a-Si:H. The material used in these experiments has proven very rough and contains pinholes. Roughness indicates variations in chemical composition and thickness, which entail variations in conductivity. Pinholes, if not properly passivated by the oxide layer, result in shunt currents. The randomness of those two factors is in agreement with the results presented in Figure 9(a). Better quality amorphous silicon will increase heating homogeneity.

The time response of the device is also an important parameter for the nature of reconfigurable operations. It was tested by serially displaying fully lighted and black images at different frequencies. The results are illustrated in Figure 10.

In these experiments, currents were measured at 2.5 V. A fully lighted image and a black image were displayed one after the other and each for the same amount of time, which varied between experiments from 1 min to 0.01 s. The device could be operated as fast as 0.05 s/image. Current was plotted against time. The curves show rounded corners that are due to capacitive effects. Those effects appear to be the time-response limiting factor. In the case of melting applications, melting takes at least half a second and will thus be the limiting time factor of reconfiguration.

Finally, although a-Si:H is known to degrade when illuminated because of light-induced defects [31], no degradation was noticed during four weeks of device operation.

5. Conclusion

In this paper, an optoelectronic-based heater is reported for the first time. It enables heating confined at microscales with low-power light pattern actuation. Optoelectronic heating (OEH) is triggered by photocurrents in the lighted parts of actuating images. Photocurrents highly respond to the operating voltage, and their dependence on the optical power input is limited. Therefore OEH efficiently operates with low-power light. Dark currents cause undesired heating in the dark regions of actuating images. Since they respond exponentially to the operating voltage, they affect resolution at higher voltages. However, dark currents can be mitigated by improving the photoconductor quality and by minimizing background illumination. The versatility of OEH has been

demonstrated by varying the size, location, and timing of the actuating light patterns. In particular, a frozen material was successfully melted within seconds. The melting areas varied from $5\text{ mm} \times 5\text{ mm}$ to $200\text{ }\mu\text{m} \times 200\text{ }\mu\text{m}$. Smaller feature sizes can be achieved by improving the resolution of OEH devices and reducing the frozen material layer's thickness. Thawing of a frozen media by OEH paves the way to the rapid fabrication and reconfiguration of microfluidic structures, as previously reported [19]. This work provides a quantitative analysis of the OEH process for further investigation of reconfigurable microfluidic circuitry controlled by low-power light images.

Acknowledgments

The authors would like to thank Drs. Hideaki Tsutsui and Eric P.Y. Chiou for their help. This work is supported by the Center for Scalable and Integrated NanoManufacturing (SINAM) (DMI-0327077).

References

- [1] E. M. Chan, R. A. Mathies, and A. P. Alivisatos, "Size-controlled growth of CdSe nanocrystals in microfluidic reactors," *Nano Letters*, vol. 3, no. 2, pp. 199–201, 2003.
- [2] D. L. Huber, R. P. Manginell, M. A. Samara, B. I. Kim, and B. C. Bunker, "Programmed adsorption and release of proteins in a microfluidic device," *Science*, vol. 301, no. 5631, pp. 352–354, 2003.
- [3] M. U. Kopp, A. J. de Mello, and A. Manz, "Chemical amplification: continuous-flow PCR on a chip," *Science*, vol. 280, no. 5366, pp. 1046–1048, 1998.
- [4] P. Sethu and C. H. Mastrangelo, "Polyethylene glycol (PEG)-based actuator for nozzle-diffuser pumps in plastic microfluidic systems," *Sensors and Actuators A*, vol. 104, no. 3, pp. 283–289, 2003.
- [5] M. E. Harmon, M. Tang, and C. W. Frank, "A microfluidic actuator based on thermoresponsive hydrogels," *Polymer*, vol. 44, no. 16, pp. 4547–4556, 2003.
- [6] N. T. Nguyen, T. H. Ting, Y. F. Yap et al., "Thermally mediated droplet formation in microchannels," *Applied Physics Letters*, vol. 91, no. 8, Article ID 084102, 2007.
- [7] D. Ross and L. E. Locascio, "Microfluidic temperature gradient focusing," *Analytical Chemistry*, vol. 74, no. 11, pp. 2556–2564, 2002.
- [8] A. A. Darhuber, J. P. Valentino, S. M. Troian, and S. Wagner, "Thermocapillary actuation of droplets on chemically patterned surfaces by programmable microheater arrays," *Journal of Microelectromechanical Systems*, vol. 12, no. 6, pp. 873–879, 2003.
- [9] Y. Liu, D. K. Cheng, G. J. Sonek, M. W. Berns, C. F. Chapman, and B. J. Tromberg, "Evidence for localized cell heating induced by infrared optical tweezers," *Biophysical Journal*, vol. 68, no. 5, pp. 2137–2144, 1995.
- [10] M. N. Slyadnev, Y. Tanaka, M. Tokeshi, and T. Kitamori, "Photothermal temperature control of a chemical reaction on a microchip using an infrared diode laser," *Analytical Chemistry*, vol. 73, no. 16, pp. 4037–4044, 2001.
- [11] S. R. Sershen, G. A. Mensing, M. Ng, N. J. Halas, D. J. Beebe, and J. L. West, "Independent optical control of microfluidic valves formed from optomechanically responsive nanocomposite hydrogels," *Advanced Materials*, vol. 17, no. 11, pp. 1366–1368, 2005.

- [12] K. Zhang, A. Jian, X. Zhang, Y. Wang, Z. Li, and H. Y. Tam, "Laser-induced thermal bubbles for microfluidic applications," *Lab on a Chip*, vol. 11, no. 7, pp. 1389–1395, 2011.
- [13] H. Yoshioka, M. Mikami, Y. Mori, and E. Tsuchida, "Synthetic hydrogel with thermoreversible gelation. I. preparation and rheological properties," *Journal of Macromolecular Science—Pure and Applied Chemistry*, vol. A31, no. 1, pp. 113–120, 1994.
- [14] H. Sugino, T. Arakawa, Y. Nara et al., "Integration in a multilayer microfluidic chip of 8 parallel cell sorters with flow control by sol-gel transition of thermoreversible gelation polymer," *Lab on a Chip*, vol. 10, no. 19, pp. 2559–2565, 2010.
- [15] M. Krishnan, J. Park, and D. Erickson, "Optothermoeological flow manipulation," *Optics Letters*, vol. 34, no. 13, pp. 1976–1978, 2009.
- [16] A. T. Ohta, A. Jamshidi, J. K. Valley, H. Y. Hsu, and M. C. Wu, "Optically actuated thermocapillary movement of gas bubbles on an absorbing substrate," *Applied Physics Letters*, vol. 91, no. 7, Article ID 074103, 2007.
- [17] P. Y. Chiou, A. T. Ohta, and M. C. Wu, "Massively parallel manipulation of single cells and microparticles using optical images," *Nature*, vol. 436, no. 7049, pp. 370–372, 2005.
- [18] P. Y. Chiou, H. Moon, H. Toshiyoshi, C. J. Kim, and M. C. Wu, "Light actuation of liquid by optoelectrowetting," *Sensors and Actuators A*, vol. 104, no. 3, pp. 222–228, 2003.
- [19] G. Haulot, A. J. Benahmed, and C. M. Ho, "Optoelectronic reconfigurable microchannels," in *Proceedings of the 24th International Conference on Micro Electro Mechanical Systems (MEMS '11)*, pp. 53–56, January 2011.
- [20] N. Attaf, M. S. Aida, and L. Hadjeris, "Thermal conductivity of hydrogenated amorphous silicon," *Solid State Communications*, vol. 120, no. 12, pp. 525–530, 2001.
- [21] H. J. Goldsmid, M. M. Kaila, and G. L. Paul, "Thermal conductivity of amorphous silicon," *Physica Status Solidi A*, vol. 76, no. 1, pp. K31–K33, 1983.
- [22] C. R. Wronski, D. E. Carlson, and R. E. Daniel, "Schottky-barrier characteristics of metal-amorphous-silicon diodes," *Applied Physics Letters*, vol. 29, no. 9, pp. 602–605, 1976.
- [23] D. E. Heller, R. M. Dawson, C. T. Malone, S. Nag, and C. R. Wronski, "Electron-transport mechanisms in metal Schottky barrier contacts to hydrogenated amorphous silicon," *Journal of Applied Physics*, vol. 72, no. 6, pp. 2377–2384, 1992.
- [24] N. Szydlo, J. Magariño, and D. Kaplan, "Post-hydrogenated chemical vapor deposited amorphous silicon Schottky diodes," *Journal of Applied Physics*, vol. 53, no. 7, pp. 5044–5051, 1982.
- [25] S. M. Sze, *Physics of Semiconductor Devices*, Wiley, 3rd edition, 2007.
- [26] T. Aoki, N. Ohru, C. Fujihashi, and K. Shimakawa, "Enhancement of non-geminate electron-hole pair recombination induced by strong electric field in hydrogenated amorphous silicon (a-Si:H): effective-temperature concept," *Philosophical Magazine Letters*, vol. 88, no. 1, pp. 9–17, 2008.
- [27] K. Jahn, R. Carius, and W. Fuhs, "Photoluminescence and photoconductivity of a-Si:H at high electric fields," *Journal of Non-Crystalline Solids*, vol. 97-98, no. 1, pp. 575–578, 1987.
- [28] W. Paul and D. A. Anderson, "Properties of amorphous hydrogenated silicon, with special emphasis on preparation by sputtering," *Solar Energy Materials*, vol. 5, no. 3, pp. 229–316, 1981.
- [29] J. A. Schmidt, R. R. Koropecski, R. D. Arce, F. A. Rubinelli, and R. H. Buitrago, "Energy-resolved photon flux dependence of the steady state photoconductivity in hydrogenated amorphous silicon: implications for the constant photocurrent method," *Thin Solid Films*, vol. 376, no. 1-2, pp. 267–274, 2000.
- [30] A. Madan, W. Czubytyj, J. Yang, M. S. Shur, and M. P. Shaw, "Observation of two modes of current transport through phosphorus-doped amorphous hydrogenated silicon Schottky barriers," *Applied Physics Letters*, vol. 40, no. 3, pp. 234–236, 1982.
- [31] T. Shimizu, "Staebler-Wronski effect in hydrogenated amorphous silicon and related alloy films," *Japanese Journal of Applied Physics Part 1*, vol. 43, no. 6 A, pp. 3257–3268, 2004.



Hindawi

Submit your manuscripts at
<http://www.hindawi.com>

